

Calibration of the optical torque wrench

Francesco Pedaci,^{1,2} Zhuangxiong Huang,^{1,2} Maarten van Oene,¹ and Nynke H. Dekker^{1,*}

¹*Department of Bionanoscience, Kavli Institute of Nanoscience, Faculty of Applied Sciences, Delft University of Technology, Lorentzweg 1, 2628 CJ Delft, The Netherlands*

²*Co-first authors*

[*n.h.dekker@tudelft.nl](mailto:n.h.dekker@tudelft.nl)

Abstract: The optical torque wrench is a laser trapping technique that expands the capability of standard optical tweezers to *torque* manipulation and measurement, using the laser linear polarization to orient tailored microscopic birefringent particles. The ability to measure torque of the order of $k_B T$ (~ 4 pN nm) is especially important in the study of biophysical systems at the molecular and cellular level. Quantitative torque measurements rely on an accurate calibration of the instrument. Here we describe and implement a set of calibration approaches for the optical torque wrench, including methods that have direct analogs in linear optical tweezers as well as introducing others that are specifically developed for the angular variables. We compare the different methods, analyze their differences, and make recommendations regarding their implementations.

© 2012 Optical Society of America

OCIS codes: (350.4855) Optical tweezers or optical manipulation; (200.4880) Optomechanics.

References and links

1. F. M. Fazal and S. M. Block, "Optical tweezers study life under tension," *Nat. Photonics* **5**, 318–321 (2011).
2. K. C. Neuman and A. Nagy, "Single-molecule force spectroscopy: optical tweezers, magnetic tweezers and atomic force microscopy," *Nat. Methods* **5**, 491–505 (2008).
3. K. Svoboda and S. M. Block, "Biological applications of optical forces," *Annu. Rev. Biophys. Biomol. Struct.* **23**, 247 (1994).
4. B. E. Funnell, T. A. Baker, and A. Kornberg, "In vitro assembly of a prepriming complex at the origin of the escherichia coli chromosome," *J. Biol. Chem.* **262**, 10327–10334 (1987).
5. L. F. Liu and J. C. Wang, "Supercoiling of the DNA template during transcription," *Proc. Natl. Acad. Sci. U.S.A.* **84**, 7024–7027 (1987).
6. M. Yoshida, E. Muneyuki, and T. Hisabori, "ATP synthase, a marvellous rotary engine of the cell," *Nat. Rev. Mol. Cell Biol.* **2**, 669–677 (2001).
7. S. Saroussi and N. Nelson, "The little we know on the structure and machinery of V-ATPase," *J. Exp. Biol.* **212**, 1604–1610 (2009).
8. Y. Sowa and R. M. Berry, "Bacterial flagellar motor," *Q. Rev. Biophys.* **41**, 103–132 (2008).
9. J. Lipfert, J. W. J. Kerssemakers, T. Jager, and N. H. Dekker, "Magnetic torque tweezers: measuring torsional stiffness in DNA and RecA-DNA filaments," *Nat. Methods* **7**, 977–980 (2010).
10. M. E. J. Friese, T. A. Nieminen, N. R. Heckenberg, and H. Rubinsztein-Dunlop, "Optical alignment and spinning of laser-trapped microscopic particles," *Nature* **394**, 348–350 (1998).
11. M. Padgett and R. Bowman, "Tweezers with a twist," *Nat. Photonics* **5**, 343–348 (2011).
12. A. Celedon, I. M. Nodelman, B. Wildt, R. Dewan, P. Searson, D. Wirtz, G. D. Bowman, and S. X. Sun, "Magnetic tweezers measurement of single molecule torque," *Nano Lett.* **9**, 1720–1725 (2009).
13. A. LaPorta and M. D. Wang, "Optical torque wrench: angular trapping, rotation, and torque detection of quartz microparticles," *Phys. Rev. Lett.* **92**, 190801 (2004).
14. J. Inman, S. Forth, and M. Wang, "Passive torque wrench and angular position detection using a single-beam optical trap," *Opt. Lett.* **35**, 2949–2951 (2010).

15. F. Pedaci, Z. Huang, M. v. Oene, S. Barland, and N. H. Dekker, "Excitable particle in an optical torque wrench," *Nat. Phys.* **7**, 259–264 (2011).
16. S. Forth, C. Deufel, M. Y. Sheinin, B. Daniels, J. P. Sethna, and M. D. Wang, "Abrupt buckling transition observed during the plectoneme formation of individual DNA molecules," *Phys. Rev. Lett.* **100**, 148301 (2008).
17. B. C. Daniels, S. Forth, M. Y. Sheinin, M. D. Wang, and J. P. Sethna, "Discontinuities at the DNA supercoiling transition," *Phys. Rev. E* **80**, 040901 (2009).
18. S. Forth, C. Deufel, S. S. Patel, and M. D. Wang, "Direct measurements of torque during Holliday junction migration," *Biophys. J.* **101**, L05–L07 (2011).
19. K. Visscher and S. M. Block, "Versatile optical traps with feedback control," *Method Enzymol.* **298**, 460–489 (1998).
20. M. Capitanio, G. Romano, R. Ballerini, M. Giuntini, F. S. Pavone, D. Dunlap, and L. Finzi, "Calibration of optical tweezers with differential interference contrast signals," *Rev. Sci. Instrum.* **73**, 1687 (2002).
21. K. Berg-Sørensen and H. Flyvbjerg, "Power spectrum analysis for optical tweezers," *Rev. Sci. Instrum.* **75**, 594–612 (2004).
22. K. C. Neuman and S. M. Block, "Optical trapping," *Rev. Sci. Instrum.* **75**, 2787–2809 (2004).
23. C. Deufel and M. D. Wang, "Detection of forces and displacements along the axial direction in an optical trap," *Biophys. J.* **90**, 657–667 (2006).
24. B. Gutierrez-Medina, J. O. L. Andreasson, W. J. Greenleaf, A. LaPorta, and S. M. Block, "An optical apparatus for rotation and trapping," *Method Enzymol.* **475**, 377–404 (2010).
25. R. Adler, "A study of locking phenomena in oscillators," *Proc. IRE* **34**, 351–357 (1946).
26. C. Deufel, S. Forth, C. R. Simmons, S. Dejgosh, and M. D. Wang, "Nanofabricated quartz cylinders for angular trapping: DNA supercoiling torque detection," *Nat. Methods* **4**, 223–225 (2007).
27. Z. Huang, F. Pedaci, M. Wiggin, M. v. Oene, and N. H. Dekker, "Electron beam fabrication of micron-scale birefringent quartz particles for use in optical trapping," *ACS Nano* **5**, 1418–1427 (2011).
28. W. J. Greenleaf, M. T. Woodside, E. A. Abbondanzieri, and S. M. Block, "Passive all-optical force clamp for high-resolution laser trapping," *Phys. Rev. Lett.* **95**, 208102 (2005).
29. O. M. Maragò, P. H. Jones, F. Bonaccorso, V. Scardaci, P. G. Gucciardi, A. G. Rozhin and A. C. Ferrari, "FemtoNewton force sensing with optically trapped nanotubes," *Nano Lett.* **8**, 3211–3216 (2008).
30. P. J. Reece, W. J. Toe, F. Wang, S. Paiman, Q. Gao, H. H. Tan, C. Jagadish, "Characterization of semiconductor nanowires using optical tweezers," *Nano Lett.* **11**, 2375–2381 (2011).
31. S. F. Tolić-Nørrelykke, E. Schäffer, J. Howard, F. S. Pavone, F. Jülicher, and H. Flyvbjerg, "Calibration of optical tweezers with positional detection in the back focal plane," *Rev. Sci. Instrum.* **77**, 103101 (2006).
32. P. Reimann, C. V. den Broeck, H. Linke, P. Hanggi, J. M. Rubi, and A. Pérez-Madrid, "Giant acceleration of free diffusion by use of tilted periodic potentials," *Phys. Rev. Lett.* **87**, 010602 (2001).
33. K. S. Asakia and S. A. Mari, "Diffusion coefficient and mobility of a brownian particle in a tilted periodic potential," *J. Phys. Soc. Jpn.* **74**, 2226–2232 (2005).
34. M. M. Tirado and J. Garciadelatorre, "Rotational-dynamics of rigid, symmetric top macromolecules; application to circular-cylinders," *J. Chem. Phys.* **73**, 198–1993 (1980).

1. Introduction

The ability of optical tweezers (OT) to manipulate microscopic particles held in the focus of a laser has paved the way for many important lines of research in fields ranging from physics to biology. In single-molecule biological physics in particular, OT is one of the techniques that have ushered in a revolution in the way biological systems can be explored. In such studies, a microscopic particle is used as a force transducer and sensor through which the optical force can be transferred to a single biopolymer (e.g. DNA, RNA or protein). This allows one to monitor e.g. the mechanical response of a single biopolymer to linear tension (force spectroscopy), or the action of enzymes that employ the tethered molecule as substrate [1–3].

In addition to force, torque also is a physical parameter of biological relevance, as shown by its role in diverse cellular processes such as DNA replication [4], transcription [5], ATP synthesis [6, 7], and bacterial propulsion [8]. However, investigating the role of torque has proved more challenging, in part due to a lack of straightforward single-molecule manipulation techniques. Fortunately, recent efforts have focused on the development of techniques that allow the control and measurement of both force and torque on microscopic actuators [9–12].

The optical torque wrench (OTW) is one such technique and distinguishes itself by its all-optical manipulation and detection of trapped microscopic birefringent particles. The OTW

can easily control and detect linear and angular displacements of trapped particles with fast μs temporal resolution, allowing one to implement fast feedback loops to actively clamp the value of force or torque [10, 13]. Recent studies have continued to expand our understanding of OTW physics by focusing on the system's angular dynamics [14, 15], but already the OTW has found applications in the study of torque-induced structural transitions of single DNA molecules [16–18]. Together, these advances demonstrate that the OTW has the potential to apply and dynamically measure torque at the scale of $k_B T$ (~ 4 pN nm), opening up new applications in the study of biophysical systems.

A key component of any trapping technique, linear or angular, is the ability to properly calibrate the instrument to perform absolute quantitative measurements. Diverse methods for the calibration of linear OT can be found in the literature [19–23], while calibration of the OTW has been less fully explored [16, 24]. Here we describe several different procedures to calibrate the angular trap of an OTW, detail their experimental implementations, and compare their outcomes. As we will show, several methods have their direct analogs in the calibration of linear traps, while others are more tailored to the particularities of angular variables.

This work is organized as follows: in section 2 we provide an overview of OTW theory (sec. 2.1) and describe our experimental system in detail (sec. 2.2); in section 3 we compare the calibration principles of OT to those of OTW; in section 4 we detail five methods for calibrating the OTW; and in section 5 we discuss their outcomes.

2. The optical torque wrench

In this section, we will describe the theoretical framework of the optical torque wrench and its experimental implementation, which together provide the necessary background for the calibration methods described subsequently.

2.1. Theoretical overview

In an OTW, torque is optically applied to a birefringent particle through spin momentum change in the linearly polarized laser field [10, 13]. Through its interaction with the birefringent material, the macroscopic polarization \vec{p} induced in the medium is in general not parallel to the laser polarization \vec{E} (Fig. 1a). Therefore the product $\vec{\tau} = \vec{p} \times \vec{E}$ is non-zero and a finite torque τ is applied to the particle. The net transferred torque is measured at the trap output as an imbalance between the intensities of the left- and right-circular components of the light that propagated inside the birefringent particle.

The torque transferred to a positive (negative) uniaxial birefringent particle is related to the angle $x = \theta_{cyl} - \theta_{pol}$ between the linear laser polarization θ_{pol} and the extraordinary (ordinary) axis θ_{cyl} according to

$$\tau = \tau_o \sin(2x). \quad (1)$$

where τ_o is the maximum optical torque, which depends on laser intensity, particle size, and birefringence [10]. For $x \ll 1$, linearization of the optical torque $\tau \simeq 2\tau_o x$ can be used to define the angular stiffness $\kappa = 2\tau_o$.

The over-damped angular equation of motion for the birefringent particle in an OTW can therefore be written as

$$-\gamma(\dot{x} + \dot{\theta}_{pol}) - \tau_o \sin(2x) + \eta(t) = 0 \quad (2)$$

where γ is the angular drag coefficient and $\eta(t)$ is the Langevin force, a Gaussian-distributed white noise term obeying $\langle \eta(t)\eta(t') \rangle = 2k_B T \gamma \delta(t - t')$.

The dynamics of the OTW are best understood by rewriting the equation of motion to make explicit the potential landscape experienced by the particle. When the laser polarization rotates at constant frequency ω (i.e. $\theta_{pol} = \omega t$), the equation of motion can be written in terms of a

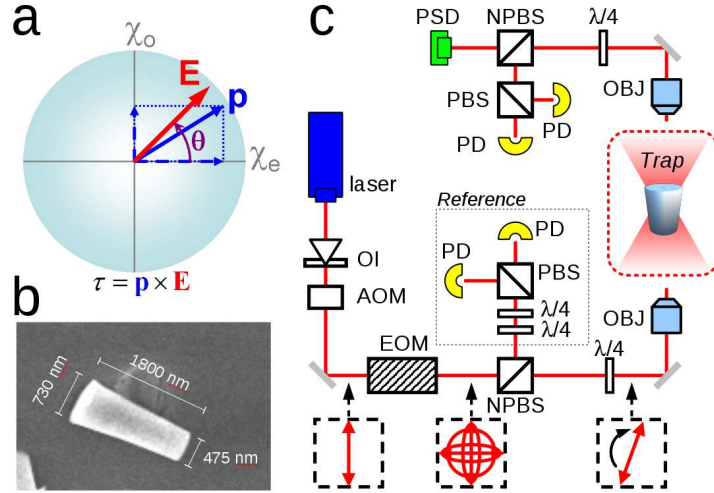


Fig. 1. Experimental configuration. **a**) Schematic depicting of the torque generation inside a birefringent crystal that has a larger susceptibility along its extraordinary axis χ_e than along its ordinary axis χ_o . **b**) SEM image of a nano-fabricated birefringent quartz cylinder used in the OTW. **c**) Diagram of the optical setup. OI: optical isolator, AOM: acousto-optic modulator, EOM: electro-optic modulator, NPBS: 50% non-polarizing beam splitter, $\lambda/4$: quarter wave-plate, PBS: polarizing beam splitter, PD: photo-detector, PSD: position sensitive detector, OBJ: 1.2NA microscope objective. The optical trap is surrounded by red dashed lines, the torque reference system is labeled and surrounded by grey dots, and the polarization state controlled by the EOM is indicated by red arrows inside the black dashed squares.

total potential $U(x) = V(x) - Fx$, where $V(x)$ is a periodic potential tilted by an external force F , as

$$\gamma\dot{x} = -U'(x) + \eta(t) \quad (3)$$

which is equivalent to Adler's equation [25]. In the OTW, the periodic angular potential takes the form of $V(x) = -\frac{\tau_o}{2} \cos(2x)$, with $V(x + \pi) = V(x)$, and the tilting force is $F = -\gamma\omega$. Hence, the result of the polarization rotation is to tilt the periodic potential.

The dynamics of the OTW can be separated into two distinct dynamic regimes, separated by a saddle-node bifurcation occurring at $\omega = \omega_c = \tau_o/\gamma$. The first regime, in which $|\omega| < \omega_c$, is characterized by the existence of a potential barrier separating two successive stable states. At these low frequencies, the drag torque $\gamma\omega$ can be balanced by the optical torque $\tau(x)$, for a particular angle x , and the particle rotates in phase with the driving polarization. When $|\omega| \lesssim \omega_c$, the presence of thermal noise can allow the system to escape the barrier between two potential minima, resulting in the appearance of regular spikes in the torque signal, a characteristic feature of the excitability of the system [15]. Physically, this corresponds to the extraordinary axis of the particle transiently slipping out of the polarization direction during rotation. In the second regime in which $|\omega| > \omega_c$, the potential barrier disappears, the stable and unstable points merge, and a limit cycle is created giving rise to a deterministic periodic torque signal with period given by

$$T_o = \frac{\pi}{\sqrt{\omega^2 - \omega_c^2}}. \quad (4)$$

In presence of noise and for ω sufficiently greater than ω_c , the period of the torque signal

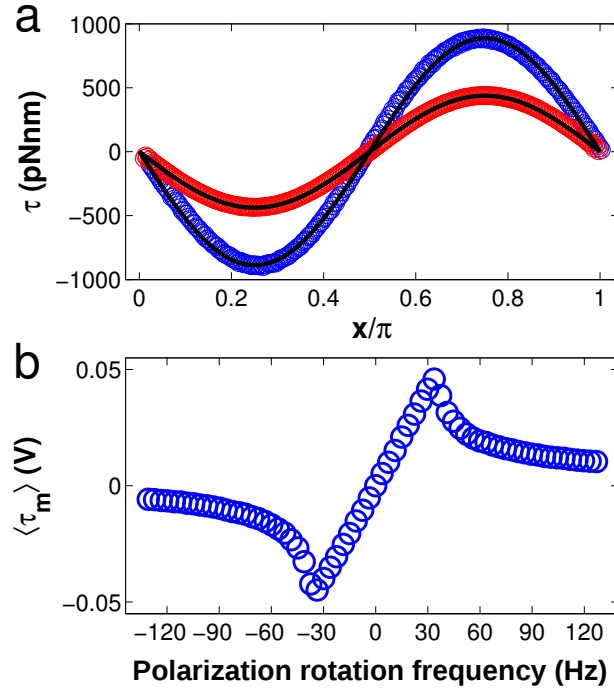


Fig. 2. Torque on a birefringent cylinder. **a)** Calibrated optical torque as a function of the angle x between the polarization and the extraordinary axis for two laser intensities (blue points: 100 mW, red points: 50 mW, power measured at the objective input). The traces are reconstructed from torque traces recorded at $\omega > \omega_c$. Calibration was performed following the method described in sec. 4.2.1. The black lines are sinusoidal fits (Eq. (1)) of the experimental points. **b)** Mean value of the measured torque as a function of the polarization rotation frequency. Within the region $|\omega| < \omega_c \simeq 37(\times 2\pi)$ Hz the torque is constant in time ($\tau_m = \beta_\tau \gamma \omega$), while for $|\omega| > \omega_c$ the torque becomes periodic, with mean period given by Eq. (4). Negative frequencies indicate opposite rotation direction. Note that the cylinder used here has a larger volume and lower ω_c than the one used in the subsequent figures and table.

becomes a statistical variable T_s distributed around its mean value T_o , hence $\langle T_s \rangle \approx T_o$.

The physics of the OTW can be experimentally verified (Fig. 2). In Fig. 2a, we demonstrate the excellent agreement between the theoretically predicted (Eq. (1)) torque τ (solid lines) and the experimentally measured values (red and blue data-points), plotted over a full period of the angle between the extraordinary axis and the laser polarization. In Fig. 2b, we plot the experimentally measured mean value of the torque transferred to the trapped birefringent cylinder (Fig. 1b) at different polarization frequencies (for experimental methods, see sec. 2.2). The transition found at $|\omega| = \omega_c$ illustrates the passage between the two dynamical regimes discussed above. For $|\omega| < \omega_c$ the torque is constant in time and its value increases linearly with the frequency to balance the drag torque. Beyond the critical frequency, the drag torque $\gamma\omega$ overcomes the maximum optical torque τ_o , and the axis of the particle escapes the direction of the rotating polarization, reducing the average value of τ_m .

2.2. Experimental configuration

In the OTW, we employ cylindrically-shaped microscopic quartz (positive uniaxial) particles [26] fabricated by electron-beam lithography [27]. The particles have a tapered profile, with the dimensions indicated in Fig. 1b, and their extraordinary axis is perpendicular to their geometrical axis. Inside the optical trap, the cylinder aligns itself parallel to the direction of laser propagation to minimize the scattering force. This, together with the three-dimensional linear trap, constrains five of the particle's degrees of freedom. The remaining degree of freedom (rotation of the cylinder around its axis) is controlled by the linear polarization of the laser, which defines the stable orientation for the extraordinary axis at $x = 0 \pmod{\pi}$ (Fig. 2a).

To control the orientation of the laser polarization, we use a fast electro optic modulator (EOM) with its axis oriented at 45° with respect to the laser polarization (Fig. 1c) in combination with a quarter wave-plate (aligned at 45° with respect to the EOM axis) [24]. The resulting polarization inside the optical trap is linear (ellipticity $\lesssim 5\%$), and its angle is linearly proportional to the voltage applied to the EOM. The torque transferred to the trapped particle is deduced from the difference of the intensity signals of the two circular components of the laser light at the output of the trap.

By applying a repetitive sawtooth signal to the EOM voltage (corresponding to a rotation between 0 and π), we can quasi-continuously rotate the polarization inside the trap. We observe that rotating the laser polarization in an empty trap generates a torque signal that is modulated at the frequency of the EOM voltage, instead of the expected constant (zero) value. This can be due to imperfections of the EOM such as a small misalignment of the internal crystals. We overcome this problem by recording a torque reference signal equivalent to the torque transferred in an empty trap (Fig. 1c, gray dotted box labeled *Reference*), and defining this as the zero-torque level. This reduces the spurious torque modulation to few percent of τ_o when a particle is trapped and rotated.

The optical trap is formed at the matched focus of a pair of identical microscope objectives (1.2 NA, water immersion). The intensity of the 1064 nm trapping laser is intentionally limited to 100 mW at the trap input. A calibrated position sensitive detector (PSD), placed in a plane conjugate to the back focal plane of the condenser, is used to monitor the displacement of the trapped particle in x,y,z. We employ an acousto-optic modulator to actively control the laser intensity, and we utilize two independent imaging systems to monitor both the laser's transverse profile at the back focal plane of the condenser as well as the surroundings of the trapped particle inside the flow cell. An FPGA card runs the feedback loops that can be used to actively control the laser intensity and the torque amplitude, while a DAQ card acquires the PSD signals. The maximum overall temporal resolution is $5 \mu\text{s}$. The flow cell is prepared with two glass slides (thickness $170 \mu\text{m}$ each) spaced by one parafilm layer, and buffer exchange is possible through inlet and outlet holes in the top glass slide.

3. Similarities and differences in the calibration of OT and OTW

In OT, quantitative force measurements can be accomplished by obtaining a complete set of three calibration parameters. First, the *sensitivity* of the detection system (in units of V/m) must be known in order to convert the measured voltage signal, proportional to the displacement of the bead inside the trap, from Volts to meters. Second, once the displacement is known in meters, the force on the trapped bead is calculated as the product between the *trap stiffness* (in units of pN/nm) and the displacement. From the analysis of the Brownian fluctuations of the particle inside the trap, one can extract the sensitivity and trap stiffness provided that the particle *drag coefficient* (in units of pN s/nm) is known. Thus in total three independent measurements are required.

The three corresponding angular parameters that need to be quantified during the calibration

of an OTW are the *torque sensitivity* β_τ (in units of V/pN nm), the *angular stiffness* κ (in units of pN nm/rad), or equivalently, the *maximum torque* τ_o (in units of pN nm), and the *angular drag coefficient* γ (in units of pN nm s).

We can nonetheless underline several differences between the calibration of OT and OTW:

(1) The quantity directly measured in an OTW is torque, from which the angle of the particle can be determined, while in OT the displacement is measured and the force is determined from it.

(2) The sensitivity in OT varies outside the linear response region of the detector. In the OTW, by contrast, the measured torque signal τ_m (in Volts) is always linearly proportional to the optical torque τ applied to the birefringent particle via the sensitivity β_τ , according to

$$\tau_m = \beta_\tau \tau. \quad (5)$$

(3) In OT, a single stable point for the position of the particle is defined and it is common (even though not necessary [28]) to employ only the region of the optical potential where the stiffness is constant and the linear approximation between force and displacement holds. In the OTW, the optical potential is periodic. This makes the anharmonic region of the angular potential readily accessible, because even when the particle explores angles far from the stable solution, it never escapes the 3D trap. In the following, to characterize the sinusoidal optical torque (Fig. 2a) we will use the maximum available torque τ_o .

(4) In both OT and OTW, when the medium viscosity is known, one has to consider how the drag coefficients depend on the particle geometry. For OT experiments, fully spherical dielectric beads with precisely known radii are readily available, hence for calibration purposes one can safely assume the theoretical value for the linear drag given by the Stokes relation (corrected for the proximity of a surface as necessary). Calibrations with other particle geometries are also possible [29, 30]. This has the advantage of reducing the number of independent calibration measurements from three to two. By contrast, for the OTW one typically nanofabricates the birefringent particles [26, 27]. We nano-fabricated quartz cylinders with $\sim 10\%$ volume variation [27] that have a lightly tapered form; due to this variability in particle size and the fact that an exact analytical expression for the drag coefficient of tapered cylinders is lacking, we develop methods that allow us to directly measure the particle drag in question. Interestingly, our experimental results find quite good agreement between the values of the measured and the theoretical drag, provided that the latter is computed for a perfect cylinder with a volume equivalent to that of the cylinders employed in the experiments.

4. Approaches for angular calibration

We now discuss different approaches to perform the three independent measurements needed for OTW calibration. The approaches have in common that they provide independent measurements of the angular thermal fluctuations, of the angular response of the system to controlled modulations of the direction of the laser polarization, and of the characteristic time-scale of the system. The interplay between these three measured quantities then serves to fix the three calibration parameters. The main experimental control parameter is the frequency ω at which the polarization is rotated, also referred to as the polarization rotation frequency (which may be zero or even negative). For convenience, we classify the different calibration methods by the number of polarization rotation frequencies employed.

4.1. Calibration approach involving measurement over the full range of frequencies: fitting the standard deviation of the torque signal

In this first approach, we rotate the laser polarization over a wide range of frequencies to probe the system's complete dynamic response while recording the torque transferred to the trapped

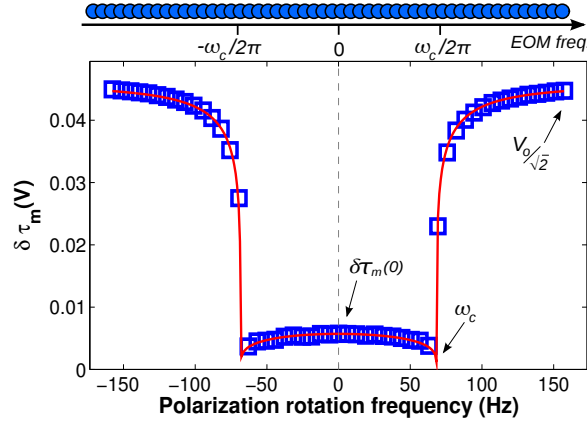


Fig. 3. Calibration approach involving measurement over the full range of frequencies. We plot the standard deviation of the measured torque (in Volts) as a function of the polarization rotation frequency. The quantities needed for calibration are indicated by arrows. The red line is a fit of the data to Eqs. (6) and (7), yielding $\omega_c = 429$ rad/s, $\delta\tau_m(0) = 5.7$ mV, and $\sqrt{2}\delta\tau_m(\infty) = V_0 = 64.9$ mV (see text). The top diagram uses blue circles to schematically indicate the polarization frequencies generated by the EOM in this method.

cylinder. For each polarization rotation frequency ω , we determine the standard deviation $\delta\tau_m$ (in Volts) of the measured optical torque signal τ_m (Fig. 3, blue squares). Similar to the data shown in Fig. 2a, an abrupt transition in the particles response at $\omega = \omega_c$ is evident.

We can derive an analytical expression for $\delta\tau_m$ (Appendix I), for which the correct form depends on whether ω is above or below the critical frequency ω_c

$$\delta\tau_m = \beta_\tau \sqrt{2\tau_o k_B T} [1 - (\omega/\omega_c)^2]^{1/4} \quad \text{for } \omega < \omega_c \quad (6)$$

$$= \beta_\tau \tau_o \left[\frac{\sqrt{(\omega/\omega_c)^2 - 1}}{(\omega/\omega_c) + \sqrt{(\omega/\omega_c)^2 - 1}} \right]^{1/2} \quad \text{for } \omega > \omega_c \quad (7)$$

Fitting the experimentally determined standard deviation of the torque to Eq. (6) and Eq. (7), as shown by the red line in Fig. 3, we obtain the complete set of calibration parameters β_τ , τ_o and $\gamma = \tau_o/\omega_c$. Alternatively, the fit can be used to find the three quantities $\delta\tau_m(\omega = 0)$, $\delta\tau_m(\omega = \infty)$ and ω_c , from which the calibration parameters can be subsequently deduced according to:

$$\tau_o = 4k_B T \delta\tau_m^2(\infty) / \delta\tau_m^2(0) \quad (8)$$

$$\gamma = \tau_o / \omega_c \quad (9)$$

$$\beta_\tau = \sqrt{2} \delta\tau_m(\infty) / \tau_o \quad (10)$$

4.2. Calibration approaches involving separate measurements at two frequencies

In this second approach, we perform separate measurements at two different polarization rotation frequencies. Within this approach, there are two variants that we describe in turn.

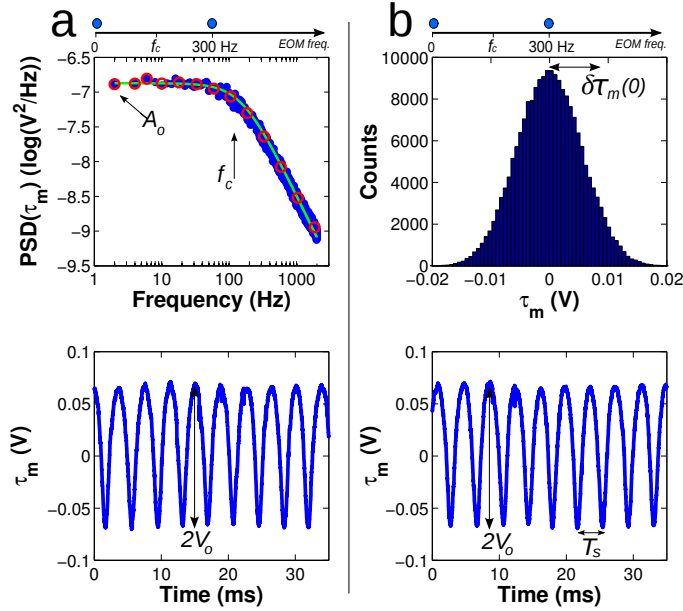


Fig. 4. Calibration approaches involving separate measurements at two frequencies. **a)** Power spectrum analysis at $\omega = 0$ followed by fast rotation at $\omega > \omega_c$. From top to bottom: a schematic of the EOM frequencies used (blue circles), the power spectrum at $\omega = 0$ (where the red points result from binning the experimental points (blue) into bins of variable size and the green line is a fit of the red points to a Lorentzian), and a segment of the torque trace acquired at $\omega/2\pi = 300\text{Hz}$. For this dataset, the measured variables (indicated by arrows) are $f_c = 152\text{ Hz}$, $A_o = 3.1\text{E-}3\text{ V}^2\text{Hz}$, and $V_o = 67\text{ mV}$. **b)** Measurement of the torque variance, period, and amplitude. From top to bottom: a schematic of the EOM frequencies used (blue circles), the probability distribution of the torque readout at $\omega = 0$, and a segment of the torque trace acquired at $\omega/2\pi = 300\text{Hz}$. For this data set, the measured variables (indicated by arrows) are $\delta\tau_m = 5.5\text{ mV}$, $\langle T_s \rangle = 3.8\text{ ms}$, and $V_o = 66\text{ mV}$.

4.2.1. Power spectrum analysis at $\omega = 0$ followed by fast polarization rotation at $\omega > \omega_c$

In this method [13], one first considers the power spectral density of the measured torque signal at $\omega = 0$, which is a measurement that yields two independent quantities (Fig. 4a). To see this, we note that at fixed laser polarization the power spectral density of the measured torque signal is described by a Lorentzian (provided that linearization around the particle's stable point is possible, i.e. $\tau_o \gg k_B T$). This Lorentzian, $P_o(\tau_m, f) = A_o/(f^2 + f_c^2)$, is parameterized by an amplitude $A_o = 4\beta_\tau^2 \tau_o^2 k_B T / (\pi^2 \gamma)$ and a corner frequency $f_c = \tau_o / (\pi \gamma) = \omega_c / \pi$. Fitting the experimental spectrum to this function therefore yields two independent variables A_o and f_c (Fig. 4a top).

To determine the third independent variable, a subsequent measurement is performed at $\omega > \omega_c$, the regime where the torque experienced by the particle is periodic as a function of time. A typical trace showing the amplitude of the torque signal V_o (defined as half of the peak-to-peak value in Volts) is shown in Fig. 4a bottom. In practice, the value of V_o can vary along the torque trace due to the small spurious modulation discussed in sec.2.2 (see also Discussion below). Therefore, to systematically determine an accurate average value of V_o from the entire recorded torque signal, we measure the standard deviation $\delta\tau_m$ and invert Eq. (7) to obtain $V_o = \beta_\tau \tau_o$.

From the measurement of the three independent variables A_o , f_c , and V_o , the calibration parameters are deduced according to:

$$\gamma = 4k_B T V_o^2 / (\pi^2 A_o) \quad (11)$$

$$\tau_o = \pi \gamma f_c \quad (12)$$

$$\beta_\tau = V_o / \tau_o \quad (13)$$

4.2.2. Calibration by measurement of the torque variance, period and amplitude

A second method that probes the response of the birefringent particle at two polarization rotation frequencies follows a similar approach. Again, we start by examining the regime in which the polarization direction is fixed ($\omega = 0$), but now we measure the standard deviation of the torque signal $\delta \tau_m(\omega = 0) = \beta_\tau \sqrt{2k_B T \tau_o}$ (Eq. (6)). This yields the first independent variable (Fig. 4b *top*).

In a subsequent step, we consider the regime in which the polarization rotation frequency is set to $\omega > \omega_c$. From the resulting periodic torque trace in the temporal domain (Fig. 4b *bottom*), we can extract the torque amplitude $V_o = \beta_\tau \tau_o$ as before. In addition we extract the mean period $\langle T_s \rangle$ of the oscillating torque experienced by the particle. Using Eq. (4), we can extract the value of $\omega_c = \tau_o / \gamma$ from $\langle T_s \rangle$.

Hence, from the measurement of the three independent variables V_o , $\langle T_s \rangle$ and $\delta \tau_m(0)$, the calibration parameters are then given by

$$\tau_o = 2k_B T [V_o / \delta \tau_m(0)]^2 \quad (14)$$

$$\gamma = \tau_o \left[\omega^2 - (\pi / \langle T_s \rangle)^2 \right]^{-\frac{1}{2}} \quad (15)$$

$$\beta_\tau = V_o / \tau_o \quad (16)$$

4.3. Calibration approaches using measurements at a single frequency

Lastly, we discuss calibration approaches that yield all three calibration parameters from a measurement performed at a single polarization rotation frequency. As we will show, the two variants presented rest on quite different theoretical approaches.

4.3.1. Sinusoidal modulation of the laser polarization direction

The first method in this category closely follows a strategy that has been used successfully for the calibration of linear traps [31]: we insert a small sinusoidal modulation of amplitude A and frequency f_{mod} into the voltage driving the EOM, which produces a polarization that oscillates about θ_{pol} at a fixed frequency: $\theta_{pol} = A \sin(2\pi f_{mod} t)$. Provided that A is sufficiently small, the power spectral density $P(\tau_m, f)$ of the measured torque τ_m experienced by the particle can be described as the sum of two components: a Lorentzian with cutoff frequency $f_c = \frac{\tau_o}{\pi \gamma}$ as in sec. 4.2.1 and, superimposed on this, a peak centered at $f = f_{mod}$. Mathematically, this is expressed as

$$P(\tau_m, f) = 2\tau_o^2 \beta_\tau^2 \left[\frac{2k_B T}{\gamma \pi^2 (f^2 + f_c^2)} + \frac{A^2}{(1 + f_c^2 / f_{mod}^2)} \delta(f - f_{mod}) \right] \quad (17)$$

Under these conditions, three independent variables can be measured from the experimental spectrum (Fig. 5a), to directly yield the three calibration parameters. First, a fit of the background power spectral density $P_o(\tau_m, f) = A_o / (f^2 + f_c^2)$ to a Lorentzian (performed excluding

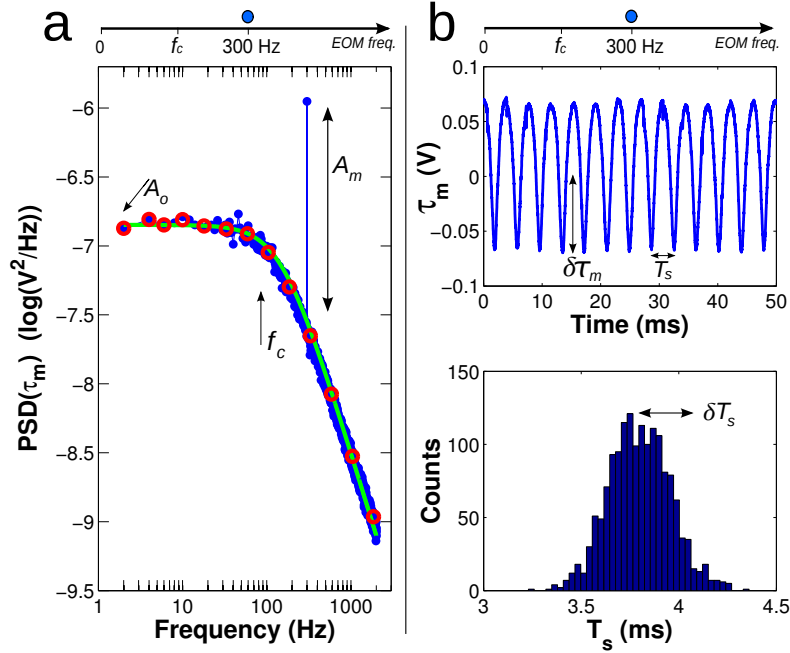


Fig. 5. Calibration approaches using measurements at a single frequency. **a)** Sinusoidal modulation of the laser polarization direction. *Top:* schematic of the EOM frequency used (the blue circle indicates the frequency of the sinusoidal modulation). *Bottom:* power spectrum of the measured torque signal including the contribution from the imposed modulation of the direction of the laser polarization ($f_{mod} = 300\text{Hz}$, $A = 0.018$ rad, $\Delta f = 2$ Hz); red points result from binning the experimental points (blue) into bins of variable size and the green line fits the red points to a Lorentzian. From the data shown, we obtain $f_c = 150$ Hz, $A_o = 3.2\text{E-}3$ V^2Hz , and $A_m = 2.18\text{E-}6$ V^2/Hz . **b)** Analysis of the diffusion in a tilted potential landscape. From top to bottom: schematic of the EOM frequency used (blue circle), a segment of the torque trace recorded at $\omega > \omega_c$, and a histogram of the measured torque period T_s . From these data, we obtain $\langle T_s \rangle = 3.8$ ms, $\delta T_s = 0.16$ ms, and $\delta \tau_m = V_o/\sqrt{2} = 45.3$ mV.

the peak at f_{mod}) provides the plateau value A_o and the cutoff frequency f_c as in sec. 4.2.1. Second, the peak power A_m at the modulation frequency, given by $A_m = P(\tau_m, f_{mod}) - P_o(\tau_m, f_{mod})$, is measured.

From the measurement of A_o , f_c , and A_m one then obtains the calibration parameters according to

$$\gamma = \frac{2k_B T A_m}{\pi^2 A^2 A_o} (1 + f_c^2 / f_{mod}^2) \Delta f \quad (18)$$

$$\tau_o = \pi \gamma f_c \quad (19)$$

$$\beta_\tau = \sqrt{\frac{A_m \Delta f}{2 \tau_o^2 A^2} (1 + f_c^2 / f_{mod}^2)} \quad (20)$$

where $\Delta f = 1/t_{msr}$ and t_{msr} is the measurement time, chosen as a multiple of the period of the applied modulation [31].

4.3.2. Analysis of the diffusion in a tilted potential landscape

A second single-frequency approach for calibration relies on detailed analysis of the diffusion of a particle in the periodic optical potential tilted by the polarization rotation (Eq. (3)).

The diffusion of a particle in a periodic potential tilted by an external force has been the object of numerous analytical and numerical studies as a result of its interesting physics and recurrence in scientific phenomena [32]. In such a system, which is at steady-state but not at the thermodynamic equilibrium, the effective diffusion coefficient D_{eff} depends on the tilt of the potential and differs from that provided by the Einstein relation $D_o = k_B T / \gamma$ [33].

In the case of the optical periodic potential $U(x)$ of the OTW, tilted by the rotation of the polarization as described by Eq. (3), the theoretical results can be effectively used for calibration. In Appendix II we show that the effective diffusion coefficient for the OTW, when $\omega > \omega_c$, can be expressed as [32]

$$D_{eff} = \frac{\pi^2 \delta T_s^2}{2 \langle T_s \rangle^3} = \frac{k_B T}{\gamma} f(r) \quad (21)$$

where δT_s^2 is the variance of the torque period and $f(r)$ is a function of $r = \omega_c / \omega$ (see Appendix II).

To carry out a calibration measurement, we fix $\omega > \omega_c$ and record the resulting periodic torque signal (Fig. 5b top). From this single time-trace, we directly measure the average value of the torque period $\langle T_s \rangle$ and its variance δT_s^2 in the temporal domain. The distribution of the period T_s is shown (Fig. 5b (bottom)). The value of ω_c can then be determined from Eq. (4) using $\omega_c = \tau_o / \gamma = \sqrt{\omega^2 - (\pi / \langle T_s \rangle)^2}$, allowing us to calculate r and $f(r)$. The drag coefficient is then found from Eq. (21) as

$$\gamma = \frac{2 k_B T \langle T_s \rangle^3}{\pi^2 \delta T_s^2} f(r) \quad (22)$$

and the maximum optical torque is then easily calculated from γ and ω_c using

$$\tau_o = \gamma \omega_c \quad (23)$$

Finally, the standard deviation of the same torque signal $\delta \tau_m$ is measured (Fig. 5), in order to yield the angular sensitivity β_τ (Eq. (7))

$$\beta_\tau = \frac{\delta \tau_m}{\tau_o} \sqrt{\frac{(\omega / \omega_c) + \sqrt{(\omega / \omega_c)^2 - 1}}{\sqrt{(\omega / \omega_c)^2 - 1}}} \quad (24)$$

5. Discussion

Using the experimental configuration described in sec. 2.2, we have experimentally implemented the five different calibration methods for the OTW described in the previous section on the same trapped birefringent cylinder. The resulting values of the calibration parameters (γ , β_τ , τ_o) are summarized in Table 1. Overall the numbers obtained with the different approaches agree well with one another. The errors shown in the table, indicated by the notation \pm_a^b , reflect the precision obtained repeating the same measurement (a) and the single measurement error that results from error propagation of experimental uncertainties in the analytical expressions (b).

For an absolute and independent check of the measurements, we can compare the experimentally determined values for the particle drag to the theoretically determined value for an appropriately-shaped cylinder (Fig. 1b). For a cylinder in water of length $1.8 \mu\text{m}$ and diameter $0.6 \mu\text{m}$, a theoretical value of $\gamma = 2.3 \text{ pN nm s}$ is expected for the drag coefficient [34], which is well within the range of experimentally measured values for γ , and therefore validates our results.

Table 1. Experimental results of the different calibration methods obtained with the same trapped birefringent cylinder. For every method, the notation $m \pm \frac{a}{b}$ indicates the mean value m , obtained in N successive measurements, the standard deviation a of the N measurements, and the error propagated from the uncertainties of the parameters measured in the method and calculated from the analytical expression of m . Here $\beta'_\tau = \beta_\tau^{-1}$. References to sections, figures and equations of this work for each method and parameter are provided.

<i>Method</i>	<i>Drag γ</i>		<i>Sensitivity β'_τ</i>		<i>Max. Torque τ_o</i>	
	(<i>pNnm s</i>)	Eq.	(<i>pNnm/mV</i>)	Eq.	(<i>pNnm</i>)	Eq.
Fit of the standard deviation of the torque ($N = 2$, sec. 4.1, Fig. 3)	$2.4 \pm \frac{0.1}{0.2}$	(9)	$15.9 \pm \frac{0.3}{0.9}$	(10)	$1041 \pm \frac{7}{63}$	(8)
Spectrum at $\omega = 0$ and fast rotation at $\omega > \omega_c$ ($N = 6$, sec. 4.2.1 Fig. 4a)	$2.1 \pm \frac{0.2}{0.3}$	(11)	$15.7 \pm \frac{0.6}{2.9}$	(13)	$1008 \pm \frac{37}{189}$	(12)
Torque variance, period and amplitude ($N = 6$, sec. 4.2.2, Fig. 4b)	$2.1 \pm \frac{0.1}{0.1}$	(15)	$16.7 \pm \frac{0.6}{0.1}$	(16)	$1100 \pm \frac{41}{25}$	(14)
Sinusoidal modulation of the polarization direction ($N = 2$, sec. 4.3.1, Fig. 5a)	$2.2 \pm \frac{0.1}{0.3}$	(18)	$16.0 \pm \frac{0.3}{2.9}$	(20)	$1044 \pm \frac{22}{129}$	(19)
Diffusion in a tilted potential landscape ($N = 6$, sec. 4.3.2, Fig. 5b)	$2.4 \pm \frac{0.1}{0.1}$	(22)	$15.9 \pm \frac{0.6}{1.4}$	(24)	$1046 \pm \frac{40}{47}$	(23)

When using these different methods, it is important to minimize potential sources of systematic errors. For example, there is a first source of error that primarily affects the methods that measure torque fluctuations during rotation of the laser polarization (sec. 4.1, 4.2, 4.3.2). This is due to the fact that it is not straightforward to obtain a torque signal that is fully free of spurious modulation (at the frequency of the EOM) in torque when $\omega > 0$, despite the improvements offered through the use of a reference signal as discussed in sec. 2.2. We find that the precise alignment of the axes of the two quarter-waveplates surrounding the optical trap is the critical parameter in achieving a flat torque signal when the polarization is rotated at a finite frequency below ω_c . Once such alignment is optimized, the residual amount of spurious torque modulation depends also on the trapped particles, probably reflecting small differences in their geometries and scattering. The data presented in this work correspond to a particle for which the spurious modulation could be reduced below the thermal noise. For other particles this was not always possible, and as a consequence the precision with which the parameters were obtained by the different methods was significantly lower (with deviations from the mean value up to $\pm 20\%$).

If the torque modulation is appreciable, the first method introduced, relying on the use of multiple frequencies (sec. 4.1) and measurement of the standard deviation of the torque, suffers from a systematic error particularly strongly. This is due to the fact that for the part of the measurement that is conducted at $0 < \omega < \omega_c$, the spurious modulation can be relatively large compared to the predicted value of the standard deviation (see Fig. 3), artificially increasing the value of $\delta\tau_m$; this effect is less pronounced when $\omega > \omega_c$.

A second source of error is the accuracy of the fit of the experimental power spectrum to the theoretical Lorentzian curve [21], affecting the two methods described in "Power spectrum

analysis at $\omega = 0$ followed by fast rotation at $\omega > \omega_c$ " (sec.4.2.1) and "Sinusoidal modulation of the laser polarization direction" (sec.4.3.1). This is reflected in the relatively large propagated uncertainty of these two methods. Variations in the fitting parameters critically depend on the weight given to different frequency regions, which can be controlled by binning the data with a variable bin size (as done in Fig. 4a and Fig. 5a to increase the weight of the Lorentzian plateau), and on the value of the maximum frequency present in the fitted spectrum, which delimits the region to which an f^{-2} -dependence is fitted.

Which type of calibration method is the be most useful to the experimentalist? Based on the above considerations of sources of error, it seems likely that the methods that rely on the analysis of torque fluctuations for $0 < \omega < \omega_c$ (sec. 4.1) and the methods that rely on spectral analysis (sec. 4.2.1 and sec. 4.3.1) should be the most prone to inaccuracies (see Table). To reduce systematic errors, one would preferably acquire and analyze torque traces in the time domain using either a fixed ($\omega = 0$) or rapidly rotating ($\omega \gg \omega_c$) polarization (methods of sec. 4.2.2 and sec. 4.3.2). On this basis, we recommend these two methods. For the practical implementation in an experimental setup, the rapidity with which calibration can be performed is also an important consideration. Amongst the methods presented here, the one based on the use of multiple polarization rotation frequencies (sec. 4.1) is surely the most time consuming; conversely, the single-frequency methods of sec. 4.3.1 and 4.3.2, which only require acquisition at a single polarization rotation frequency, are the most rapid. When high throughput is required, these two methods are preferred. Taking both speed and accuracy into account, we conclude that the single-frequency method of sec. 4.3.2 will be typically the most suitable. This method also has the advantage of allowing one to dynamically measure possible variations of the drag coefficient within few polarization cycles, which can be useful in micro-rheology measurements.

In conclusion, we have described and performed various methods of OTW calibration, some with direct OT analog and others developed specifically for the angular variables. Overall, the different methods lead to close results, which also agree with the theoretical prediction for the particle drag coefficient. However, the absolute values of the variables measured by the instrument should be expected to depend on the details of calibration method chosen. We hope this work can contribute to a wider use of the OTW, a versatile technique with many potential applications in physical and biophysical studies.

Appendix I: Derivation of the standard deviation of the torque

We derive here the analytical expressions (Eq. (6) and Eq. (7)) for the standard deviation of the torque (sec. 4.1). We recall that $\tau_m = \beta_\tau \tau$ (Eq. (5)), where τ_m is the measured torque signal in Volts, β_τ is the sensitivity, $\tau = \tau_o \sin(2x)$ is the optical torque (Eq. (1)), and x is the angle between the laser polarization and the extraordinary axis of the birefringent cylinder. When the laser polarization rotates at a constant frequency ω , the noise-free equation of motion can be written as

$$\dot{x} = -\frac{\tau_0}{\gamma} \sin(2x) - \omega \quad (25)$$

(see Eq. (3)). We treat the two cases $\omega < \omega_c$ and $\omega > \omega_c$ separately.

For $\omega < \omega_c = \tau_o/\gamma$, the cylinder rotates in phase with the polarization. At equilibrium, when $x = x_{eq}$, the mean torque is given by

$$\langle \tau \rangle = -\tau_o \sin(2x_{eq}) = \gamma\omega \quad (26)$$

from which we deduce the equilibrium position $x_{eq} = \frac{1}{2} \arcsin(\frac{\omega}{\omega_c})$. We can express the variance of x from the equipartition theorem as $\delta x^2 = k_B T / \kappa$, where the angular stiffness κ can be

written as $\kappa = -(\partial\tau/\partial x)_{eq} = 2\tau_o \cos(2x_{eq})$. This allows us to write the variance of the torque (see Eq. (28)) as

$$\delta\tau^2 = \left(\frac{\partial\tau}{\partial x}\right)^2 \delta x^2 = 2k_B T \tau_o \cos(2x_{eq}) \quad (27)$$

$$= 2k_B T \tau_o \sqrt{1 - (\omega/\omega_c)^2} \quad (28)$$

Equation (6) is obtained from Eq. (28) by multiplying by the sensitivity β_τ .

For $\omega > \omega_c$, the cylinder does not rotate in phase with the driving polarization, and the noise-free solution is a periodic torque trace with period T_o given by Eq. (4). In this case, the mean value of the torque is given by

$$\begin{aligned} \langle\tau\rangle &= \frac{1}{T_o} \int_0^{T_o} \tau dt = \frac{1}{T_o} \int_0^{T_o} \gamma(\dot{x} + \omega) dt \\ &= \frac{1}{T_o} \gamma[x(T_o) - x(0)] + \gamma\omega = -\frac{1}{T_o} \gamma\pi + \gamma\omega \\ &= \gamma\left(\omega - \sqrt{\omega^2 - \omega_c^2}\right) \end{aligned} \quad (29)$$

The expression of $\langle\tau\rangle$ is then used to calculate the torque variance $\delta\tau^2$ according to

$$\delta\tau^2 = \langle\tau^2\rangle - \langle\tau\rangle^2 = \frac{1}{T_\tau} \int_0^{T_\tau} \tau\gamma(dx/dt + \omega) dt - \langle\tau\rangle^2 = \gamma\omega \langle\tau\rangle - \langle\tau\rangle^2 \quad (30)$$

$$= \tau_o^2 \frac{\sqrt{(\omega/\omega_c)^2 - 1}}{(\omega/\omega_c) + \sqrt{(\omega/\omega_c)^2 - 1}} \quad (31)$$

Equation (7) is obtained from Eq. (31) by multiplying by the sensitivity β_τ .

Appendix II: Diffusion in a tilted periodic potential

We discuss here the theoretical results used in the calibration method based on analysis of the diffusion of a particle in a tilted periodic potential (sec. 4.3.2). Specifically, we consider the diffusion in a total potential $U(x) = V(x) - Fx$ formed by a periodic potential $V(x)$, tilted by an external force F . In the case of the OTW, the motion of the over-damped particle is described by Eq. (3).

When the polarization rotation frequency is set to $\omega > \omega_c$, the system is far from the thermodynamic equilibrium as there is a non-zero probability flux resulting from the disappearance of the energy barrier between successive minima. In this case, the Einstein relation $D_o - \mu k_B T = 0$ (expressed in terms of the mobility $\mu = 1/\gamma$) is not valid. Rather, the following approximate expression can be derived for the effective values of the diffusion coefficient D_{eff} and the effective mobility μ_{eff} , provided $\gamma\omega \gg k_B T$ [33]:

$$D_{eff} - k_B T \mu_{eff} \approx \frac{k_B T}{\gamma} \frac{\sqrt{\omega^2 - \omega_c^2}}{\omega} \left[\frac{2\langle\tau^2\rangle}{\gamma^2 \omega^2} + \frac{5\langle\tau^3\rangle}{\gamma^3 \omega^3} \right] \quad (32)$$

The effective mobility is in general defined by $\mu_{eff} = dv/dF$ [33], where v is the speed of the particle under the action of the force F . In our case, recalling that for $\omega > \omega_c$ the torque is a periodic function of time with period $\langle T_s \rangle$ (Eq. (4)) and $F = -\gamma\omega$ (Eq. (3)), the effective mobility can be expressed as

$$\mu_{eff} = -\frac{1}{\gamma} \frac{d}{d\omega} \langle v(\omega) \rangle = \frac{1}{\gamma} \frac{d}{d\omega} \frac{\pi}{\langle T_s \rangle} \approx \frac{\omega}{\gamma \sqrt{\omega^2 - \omega_c^2}} \quad (33)$$

Next, we use the expressions for $\langle \tau^2 \rangle$ (see Eq. (30)), and derive $\langle \tau^3 \rangle = -(\gamma/2)\tau_0^2\sqrt{\omega^2 - \omega_c^2} + \gamma^3\omega^2(\omega - \sqrt{\omega^2 - \omega_c^2})$. Substituting these expressions together with with Eq. (33) into Eq. (32), we find that the effective diffusion coefficient can be written as

$$D_{eff} = \frac{k_B T}{\gamma} f(r) \quad (34)$$

where $r = \frac{\omega_c}{\omega}$ and where $f(r)$ is given by

$$f(r) \approx \frac{1}{\sqrt{1-r^2}} + \frac{2\sqrt{1-r^2}}{1+\sqrt{1-r^2}} \left[r^2 + \frac{5}{4}r^4 \left(1 + \frac{1}{1+\sqrt{1-r^2}} \right) \right]. \quad (35)$$

Acknowledgments

We thank J. Lipfert and M. Versteegh for fruitful discussions, J. van der Does, D. de Roos and J. Beekman for help with instrumentation and infrastructure, and TU Delft, FOM (Dutch Foundation for Research on Matter), and the European Science Foundation for financial support.